Earth and Planetary Science Letters 449 (2016) 48–60

Contents lists available at ScienceDirect

Earth and Planetary Science Letters

www.elsevier.com/locate/epsl

Upper mantle shear wave velocity structure beneath northern Victoria Land, Antarctica: Volcanism and uplift in the northern Transantarctic Mountains

Jordan H. Graw [a,*], Aubreya N. Adams [b], Samantha E. Hansen [a], Douglas A. Wiens [c], Lauren Hackworth [a], Yongcheol Park [d]

[a] Department of Geological Sciences, The University of Alabama, Tuscaloosa, AL, USA
[b] Department of Geology, Colgate University, Hamilton, NY, USA
[c] Department of Earth and Planetary Sciences, Washington University in St. Louis, St. Louis, MO, USA
[d] Korea Polar Research Institute, Incheon, Republic of Korea

ARTICLE INFO

Article history:
Received 12 February 2016
Received in revised form 3 May 2016
Accepted 20 May 2016
Available online xxxx
Editor: P. Shearer

Keywords:
seismology
tectonophysics
Antarctica
surface wave tomography
geodynamics

ABSTRACT

The Transantarctic Mountains (TAMs) are the largest non-compressional mountain range on Earth, and while a variety of uplift mechanisms have been proposed, the origin of the TAMs is still a matter of great debate. Most previous seismic investigations of the TAMs have focused on a central portion of the mountain range, near Ross Island, providing little along-strike constraint on the upper mantle structure, which is needed to better assess competing uplift models. Using data recorded by the recently deployed Transantarctic Mountains Northern Network, as well as data from the Transantarctic Mountains Seismic Experiment and from five stations operated by the Korea Polar Research Institute, we investigate the upper mantle structure beneath a previously unexplored portion of the mountain range. Rayleigh wave phase velocities are calculated using a two-plane wave approximation and are inverted for shear wave velocity structure. Our model shows a low velocity zone (LVZ; ~4.24 km s^{-1}) at ~160 km depth offshore and adjacent to Mt. Melbourne. This LVZ extends inland and vertically upwards, with more lateral coverage above ~100 km depth beneath the northern TAMs and Victoria Land. A prominent LVZ (~4.16–4.24 km s^{-1}) also exists at ~150 km depth beneath Ross Island, which agrees with previous results in the TAMs near the McMurdo Dry Valleys, and relatively slow velocities (~4.24–4.32 km s^{-1}) along the Terror Rift connect the low velocity anomalies. We propose that the LVZs reflect rift-related decompression melting and provide thermally buoyant support for the TAMs uplift, consistent with proposed flexural models. We also suggest that heating, and hence uplift, along the mountain front is not uniform and that the shallower LVZ beneath northern Victoria Land provides greater thermal support, leading to higher bedrock topography in the northern TAMs. Young (0–15 Ma) volcanic rocks associated with the Hallett and the Erebus Volcanic Provinces are situated directly above the imaged LVZs, suggesting that these anomalies are also the source of Cenozoic volcanic rocks throughout the study area.

1. Introduction

With a length of ~4000 km and elevations up to ~4500 m, the Transantarctic Mountains (TAMs) separate old craton beneath East Antarctica from rifting beneath West Antarctica (Fig. 1). Exposed TAMs bedrock within the McMurdo Dry Valleys exhibits Precambrian to Early Paleozoic metamorphic rocks associated with the Ross Orogeny, overlain by subhorizontal sedimentary beds of the Devonian to Triassic Beacon Supergroup (Barrett, 1991; Borg et al., 1990). Apatite fission track data sequence three main phases of uplift associated with the TAMs: Early Cretaceous, Late Cretaceous, and Early Cenozoic. The most significant exhumation occurred ~55 Ma, and it is thought that the most substantial uplift for the TAMs occurred during this time (Fitzgerald, 2002). However, the TAMs show no evidence of folding or reverse faulting associated with traditional mountain building. This lack of compressional structures makes characterization of the TAMs tectonic history difficult, and a number of uplift mechanisms have been proposed.

* Corresponding author.
E-mail address: jhgraw@crimson.ua.edu (J.H. Graw).

http://dx.doi.org/10.1016/j.epsl.2016.05.026
0012-821X/

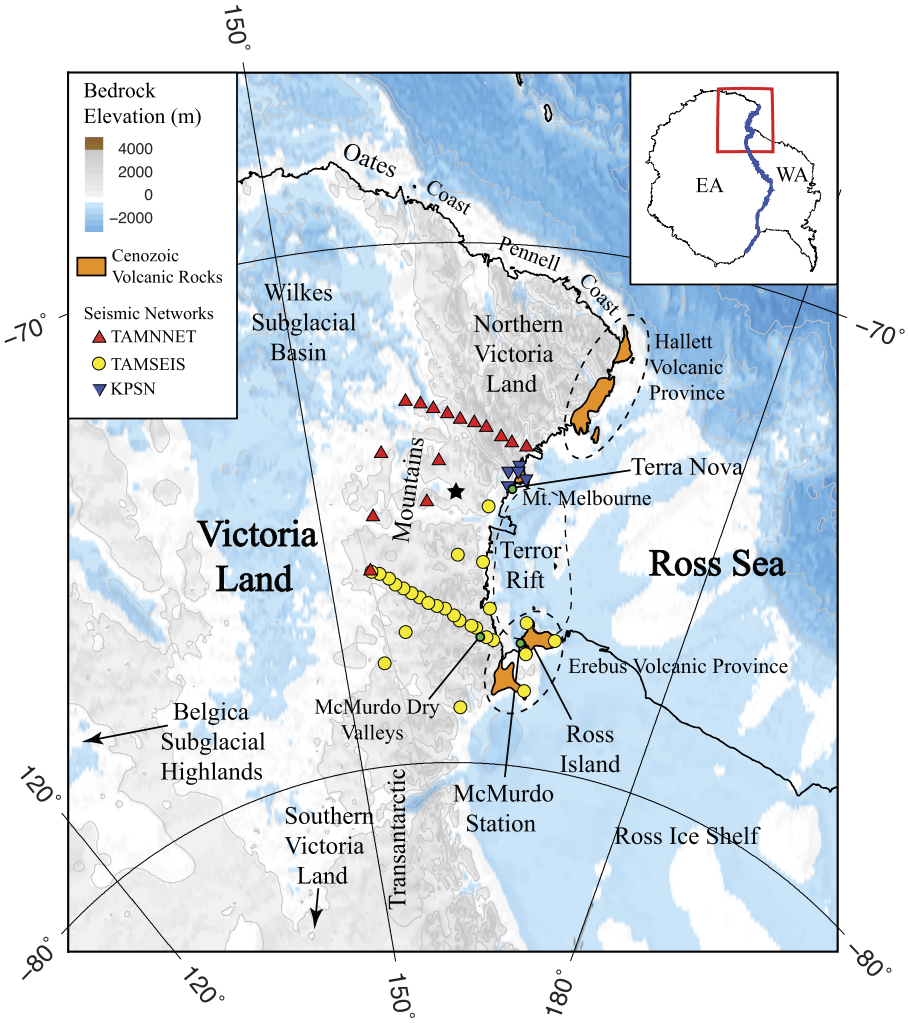

Fig. 1. Overview of the study area. Topographic bedrock elevations are from the BEDMAP2 model (Fretwell et al., 2013). Orange shading indicates areas of exposed Cenozoic volcanic rocks (Storti et al., 2008; Di Vincenzo et al., 2010). Red triangles indicate TAMNNET stations, yellow circles indicate TAMSEIS stations, and inverted purple triangles indicate KPSN stations. The black star marks the location where the partial derivatives were calculated. (Inset) Outline of Antarctica, with the red box highlighting the study region. The blue line is the boundary between East Antarctica (EA) and West Antarctica (WA). (For interpretation of the references to color in this figure, the reader is referred to the web version of this article.)

Stern and ten Brink (1989) and ten Brink et al. (1997) modeled subglacial topography from seismic and radar surveys as well as gravity data, and they suggested that the TAMs resulted from upward flexure of the free-edge of the East Antarctic craton, made possible by thermal conduction from its juxtaposition to the West Antarctic Rift System (WARS). This implies that there is hotter mantle beneath the hypothesized thinner crust of the WARS. This flexural model also includes an erosional component, correlated with isostatic rebound, which also aids uplift (Stern and ten Brink, 1989; ten Brink et al., 1997). In contrast, Studinger et al. (2004) and Karner et al. (2005), who modeled aerogeophysical and shipboard gravity data, respectively, offer a different uplift mechanism for the TAMs. Both studies suggest that the TAMs resulted from basin subsidence and rift flank uplift, associated with climate-inducing erosional unloading. Instead of a thermal load, this uplift mechanism requires a thick crustal root beneath the TAMs to provide isostatic buoyancy (Studinger et al., 2004; Karner et al., 2005). Other studies have also advocated for a crustal root, possibly resulting from the extensional collapse of thickened crust in West Antarctica (Bialas et al., 2007; Huerta and Harry, 2007). Alternatively, Lawrence et al. (2006), who jointly inverted P-wave receiver functions with Rayleigh wave phase velocities, suggested a hybrid model that includes a combination of erosional unloading, thermal buoyancy, and local crustal isostasy.

The distribution of exposed volcanic rocks may also provide some evidence to understand the TAMs uplift. Cenozoic volcanic rocks are found both in the vicinity of Mt. Erebus and north of Mt. Melbourne, throughout northern Victoria Land (Fig. 1; Storti et al., 2008; Di Vincenzo et al., 2010). However, no such volcanic rocks are present within the section of the TAMs adjacent to the Terror Rift. Numerous geochemical studies have attempted to characterize the source of these volcanic rocks, but conflicting results have yielded no consensus on their origin (Kyle, 1990; Rocholl et al., 1995; Orlando et al., 2000). Different isotopic signatures have suggested the following possibilities: (1) an enriched mantle source, which is indicative of early-stage rifting, (2) a depleted mantle source, which has a stronger component of melt and is generally attributed to a developed rift system, and (3) a HIMU (or High μ, where $\mu = (^{238}U/^{204}Pb)_{t=0}$) mantle source, which is generally associated with deep plumes (Rocholl et al., 1995). Identifying the source of these volcanic rocks could provide further evidence on what mechanisms contribute to the TAMs uplift.

Previous regional studies have investigated the seismic structure beneath the TAMs to try to differentiate between the proposed uplift mechanisms; however, given the distribution of stations, most of these studies have focused on a central portion of the TAMs, near Ross Island (Fig. 1). For instance, using P-wave receiver functions, Bannister et al. (2003) investigated the crustal

structure and found thin crust (∼18–20 km) beneath the Ross Sea coastline, thickening inland (∼36–40 km) beneath the mountain range. Similar results were found by Lawrence et al. (2006), but this study also found an average crustal thickness beneath East Antarctica of ∼35 km, suggesting that the TAMs are underlain by a ∼5 km thick crustal root. In contrast, Hansen et al. (2009) modeled S-wave receiver functions and Rayleigh wave group velocities and found little to no evidence for a crustal root in this area. Hansen et al. (2016), who also used S-wave receiver functions, recently provided constraints on the crustal structure beneath the northern TAMs. They find that while slightly thicker crust may be locally observed, it is not a consistent, along-strike feature beneath the mountain range, suggesting that crustal buoyancy does not significantly contribute to the TAMs uplift.

The upper mantle seismic structure beneath the TAMs has also been investigated in relation to the proposed uplift mechanisms. Regional body and surface wave tomography models show slow upper mantle velocities beneath the Ross Sea, concentrated beneath Mt. Erebus, the Terror Rift, and the McMurdo Dry Valleys (Fig. 1; Watson et al., 2006; Lawrence et al., 2006). These slow velocities extend to ∼300 km depth, and there is a transition to faster upper mantle velocities ∼50–100 km inland beneath the adjacent TAMs. The slow velocities have been interpreted as warm, buoyant upper mantle associated with the WARS. However, the regional models (Watson et al., 2006; Lawrence et al., 2006) lose resolution away from Ross Island, particularly north of Terra Nova Bay, making it difficult to determine the lateral extent of the low velocities. Beneath the northern TAMs, the only available upper mantle velocity constraints are from global- and continental-scale tomographic models (*e.g.*, Morelli and Danesi, 2004; Ritzwoller et al., 2001; Sieminski et al., 2003; Hansen et al., 2014), which have a horizontal resolution of ∼600–1000 km. Therefore, our ability to evaluate along-strike upper mantle variations, particularly beneath the northern TAMs, is limited.

In this study, we provide further along-strike characterization of the upper mantle structure beneath the TAMs to better assess competing uplift models and to identify the source of young volcanic rocks exposed at the surface. We utilize Rayleigh wave data and a two-plane wave method to generate phase velocity maps beneath the northern TAMs. The resulting dispersion curves are inverted to model the corresponding shear wave velocity structure in the upper mantle. Most of our data were recorded by the recently deployed Transantarctic Mountains Northern Network (TAMNNET; Fig. 1), which fills a gap in the seismic coverage of Antarctica and offers the capability to study a previously unexplored portion of the TAMs (Hansen et al., 2015). Our model helps to elucidate the lateral extent of the slow upper mantle velocities observed in previous studies (Watson et al., 2006; Lawrence et al., 2006) and what role these anomalies play in the TAMs uplift.

2. Data and methodology

2.1. Data

The TAMNNET array was deployed during the Summer 2012 Antarctic field season and included 15 polar-rated broadband seismometers (Fig. 1; Hansen et al., 2015). Ten stations were oriented in a transect perpendicular to the northern TAMs, with the five remaining stations evenly distributed inland behind the TAMs front, further to the south. It is worth noting that station KNYN, the southernmost station, reoccupied a site previously associated with the Transantarctic Mountains Seismic Experiment (TAMSEIS; Fig. 1). The TAMNNET station configuration allows for adequate coverage to investigate the upper mantle structure beneath the northern TAMs. However, to further increase resolution within our study area, data from several TAMSEIS stations as well as data from a small, five-station array near Mt. Melbourne (KPSN), which is operated by the Korea Polar Research Institute (Fig. 1; Park et al., 2014), were also incorporated into our analysis. All TAMNNET and KPSN data were recorded between December 2012 and November 2014, while data from TAMSEIS (which only recorded during austral summer months) were recorded between December 2000 and December 2003. Events used in our study lie within epicentral distances of 30–150° (Fig. 2), with no constraint on depth. A minimum moment magnitude of 4.5 was chosen for epicentral distances of 30–60°, with a minimum magnitude of 5.5 for distances of 60–150°. This approach was taken in order to capture the smaller, more numerous earthquakes that occur at and around the circum-Antarctic ridge system. In total, 877 events met our criteria. This dataset provides good azimuthal coverage, barring a back-azimuth gap between ∼30–80° associated with the seismically inactive central Pacific (Fig. 2). The TAMNNET/KPSN dataset contained nearly twice the number of events when compared to the TAMSEIS dataset. Therefore, the TAMSEIS data was given twice the weight throughout the entire inversion process.

Each seismogram was pre-processed by filtering the waveform at 25 different periods, ranging from 18 to 182 s. Fig. 3 shows an example of the raypath density at 43 s period. Waveforms were quality checked for low signal-to-noise ratio, significant beating, and interfering phases. A window slightly larger than the Rayleigh wave was used in order to adequately capture the arrival and entirety of the fundamental-mode Rayleigh waveform. Phase and amplitude data were obtained through Fourier analysis of each windowed signal, which were then used in the phase velocity inversion algorithm.

2.2. Phase velocity inversion

Established surface wave tomography methods treat the incoming raypath as a plane wave traveling along a great-circle path (Forsyth and Li, 2005; Li et al., 2003). However, this technique does not account for lateral heterogeneities along the path of propagation. Given this, we instead employed a two-plane wave method that models the incoming wavefield as the interference of two plane waves (Forsyth and Li, 2005). This approach is advantageous to other phase velocity inversion methods because it accounts for off great-circle path effects, scattering, and velocity heterogeneities between the source and receiver. The inversion, overall, was performed in two stages: (1) a simulated annealing inversion of the fundamental Rayleigh wave, which yields the best wave parameters for a given event, and (2) a linear inversion of the resultant wave parameters for phase velocity perturbations (Forsyth and Li, 2005).

To encompass the TAMNNET, TAMSEIS, and KPSN arrays, a grid of 644 nodes was generated. The inner node spacing is 0.5°, and the outer node spacing is 1.0°. An *a priori* damping coefficient was applied to each node, which controls the degree to which the resulting model can deviate from the starting model. A range of damping parameters, from 0.10 to 0.20 km s^{-1} with a 0.05 km s^{-1} interval, was tested, and we found that a damping parameter of 0.15 km s^{-1} for the inner nodes provided the best results. This damping parameter lead to phase velocity maps with the lowest uncertainty and allowed velocity contrasts to vary, without being overly restrictive. The damping parameter for the outer nodes was chosen to be 10 times greater than that of the inner grid nodes (1.5 km s^{-1}). This increase in damping was applied so that the outer nodes absorb wavefield anomalies that the two-plane wave method cannot account for Forsyth and Li (2005), Yang and Forsyth (2006a).

Using a starting model based on the AK-135 reference Earth model (Kennett et al., 1995), we performed an inversion to obtain

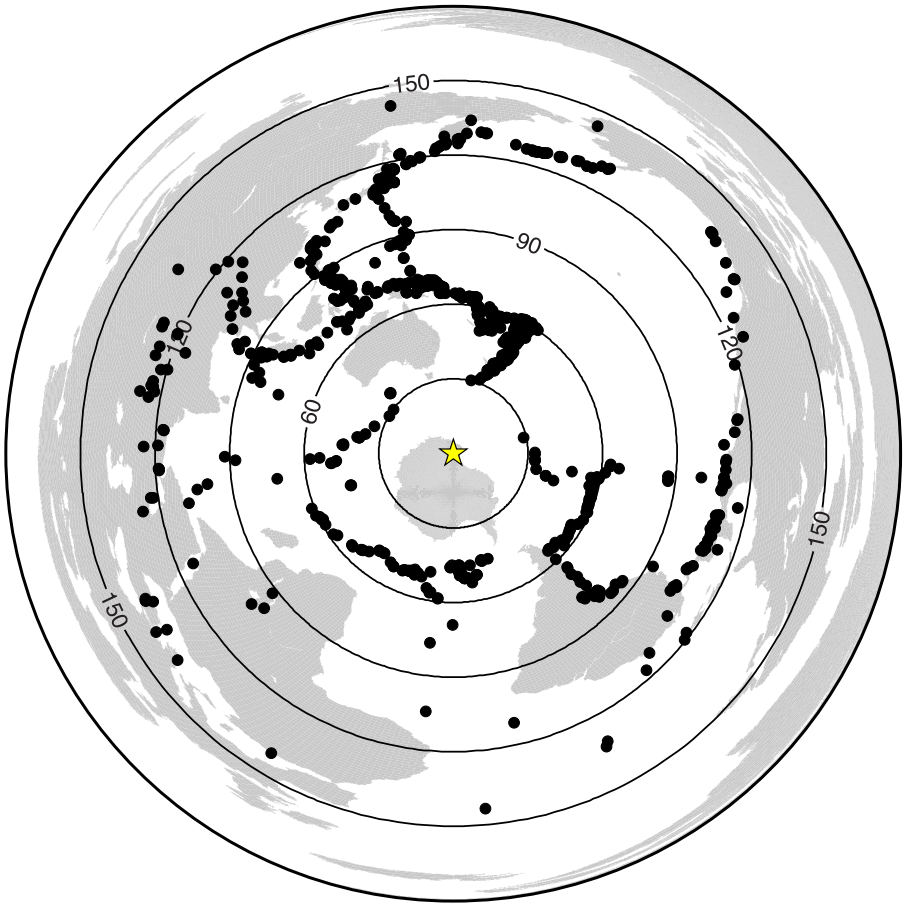

Fig. 2. Map showing the locations of all events (black dots) used in our study. The yellow star marks the center of the TAMNNET array. Concentric circles mark the epicentral distance in 30° increments from the yellow star. All events lie within 30–150° from the examined stations. (For interpretation of the references to color in this figure, the reader is referred to the web version of this article.)

a 1-D dispersion curve that represents the entire study area. It is worth noting that this initial inversion was performed with a variety of starting models, but in each case, the inversion converged to the same 1-D phase velocity curve, regardless of the initial input. The 1-D phase velocity curve was used as the starting model for the 2-D phase velocity inversion at each grid node.

A Gaussian sensitivity function was also applied during the initial 1-D stage of the inversion as well as in the 2-D inversion for phase velocity. This function was used to account for lateral heterogeneities off the great-circle path (Yang and Forsyth, 2006b). A suite of Gaussian widths were investigated, ranging from 45 to 100 km, and we found that a width of 80 km allows for enough variation in the resulting models without causing unrealistic velocity structure at depth. An inherent problem with the Gaussian sensitivity function is that it can only account for subsurface structure if the wavelength of the desired period is larger than that structure (Zhou et al., 2004; Yang and Forsyth, 2006b). To counteract this, finite frequency sensitivity kernels were developed for both the phase and amplitude of the surface waves (Zhou et al., 2004). Yang and Forsyth (2006a, 2006b), for instance, showed how incorporating finite frequency sensitivity kernels into their surface wave tomography improved resolution of smaller-scale structure at shorter periods. Therefore, we also included the finite frequency sensitivity kernels in our 2-D phase velocity inversion.

2.3. Shear wave velocity inversion

For each of our inner grid nodes, we inverted the phase velocity dispersion curve for a 1-D shear velocity profile. Our representative phase velocity dispersion curve spans periods of 18 to 103 s. The longest period phase velocities (>103 s) were not used because their wavelengths approach the size of our array, they have larger uncertainties, and resolution tests indicate that they are poorly resolved compared to the shorter period data. The inversion methodology was developed by Julià et al. (2000) and was created primarily as a joint inversion of dispersion data and receiver functions. The inversion scheme uses a damped, generalized linear least-squares technique with a weight coefficient that controls the trade-off between dispersion and receiver function influence. We simply maximize the dispersion data influence factor, thus removing the receiver function input. 1-D shear velocity profiles at a given depth can be smoothed with a Gaussian weighted smoothing parameter, creating a pseudo 3-D shear velocity model (Adams et al., 2012). Smoothing of the shear velocity profiles was investigated by creating maps at three different smoothing lengths (60, 80, and 100 km) and observing the effects on the resultant models. In order to maintain realistic lateral velocity contrasts, while not over-smoothing the data, a characteristic smoothing length of 80 km was used.

A step-wise representation of the Preliminary Reference Earth Model (PREM) (Dziewonski and Anderson, 1981), with *a priori* crustal thickness constraints from Hansen et al. (2016), was used as the initial model for each grid node. Models were held fixed within the crust and below 300 km depth. Each layer has an individual smoothing parameter associated with it, which inhibits large and unrealistic contrasts in velocity within a given layer. Performing the inversion with various crustal thicknesses shows that the structure within ~20 km below the Moho is not well resolved. However, all models converge below this depth, regardless

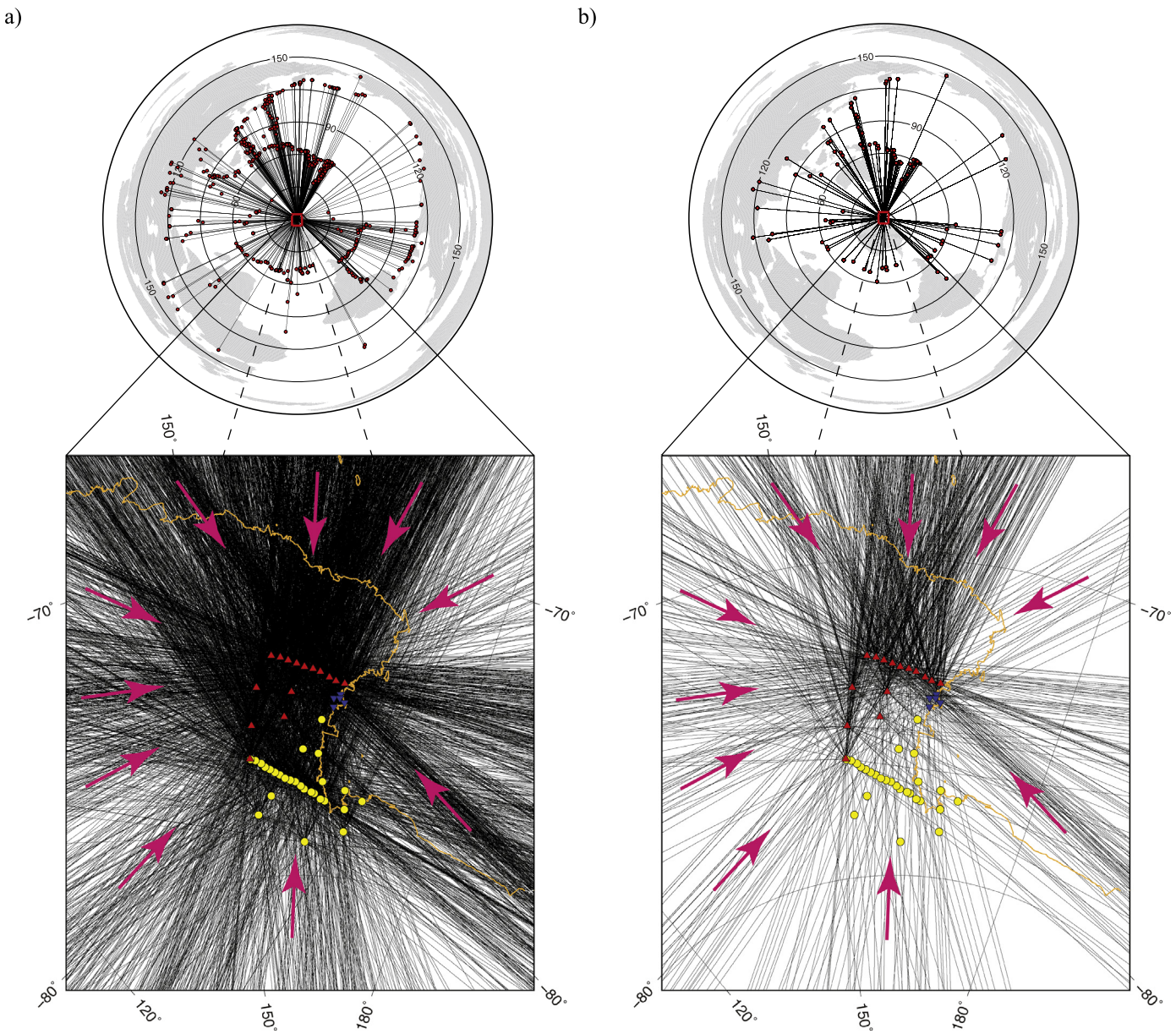

Fig. 3. Example ray path coverage maps for 43 s Rayleigh waves. Station symbols are the same as in Fig. 1. Magenta arrows show the dominant direction of ray path propagation. The images on top show earthquake locations and the paths of propagation to the study area, indicated by the red box. The bottom images show the incoming ray paths, terminating at each station. (a) Ray path coverage map using all 413 events associated with 43 s period. (b) Ray path coverage map constructed by randomly de-sampling the full dataset to 109 events to better illustrate the dominant directions of propagation across the study area. (For interpretation of the references to color in this figure, the reader is referred to the web version of this article.)

of crustal input constraints. Therefore, we interpret results beginning at ∼60 km depth. Following the method of Yu and Mitchell (1979), Rayleigh wave phase partial derivatives, with respect to shear wave velocity at varying depths and frequencies, were calculated in order to assess the maximum depth that can be resolved by our model (Fig. 4). This assessment was performed using a central point in our study area since it lies within a zone of dense raypath coverage (Fig. 1). The maximum depth resolved by our model is ∼160 km. The 103 s period is capable of resolving structure at this depth, and may also resolve deeper structure; however, shear velocity maps created at depths >∼160 km repeat the same heterogeneity as that seen at ∼160 km. This could be due to a lack of long period data or simply could reflect that lateral velocity variations are minimal at these depths. The long peak on the partial derivative for the 103 s period (Fig. 4) is credited to the shortage of long period data available, thereby creating a peak with a poor termination point. Therefore, our interpretations are limited to depths at and above ∼160 km. A uniform vertical smoothing parameter was applied to the entire velocity model in order to avoid large and unrealistic velocity contrasts across boundary layers. We performed a suite of inversions at each node, using an array of uniform smoothing parameters from 2 to 1000. The best trade-off between data curve fitting and realistic velocity perturbations within the velocity profile was found with a smoothing parameter of 15 (Fig. 5).

3. Results

3.1. Phase velocities and resolution tests

Fig. 6 shows examples of the generated phase velocity maps. The phase velocities are plotted as percent deviations from the

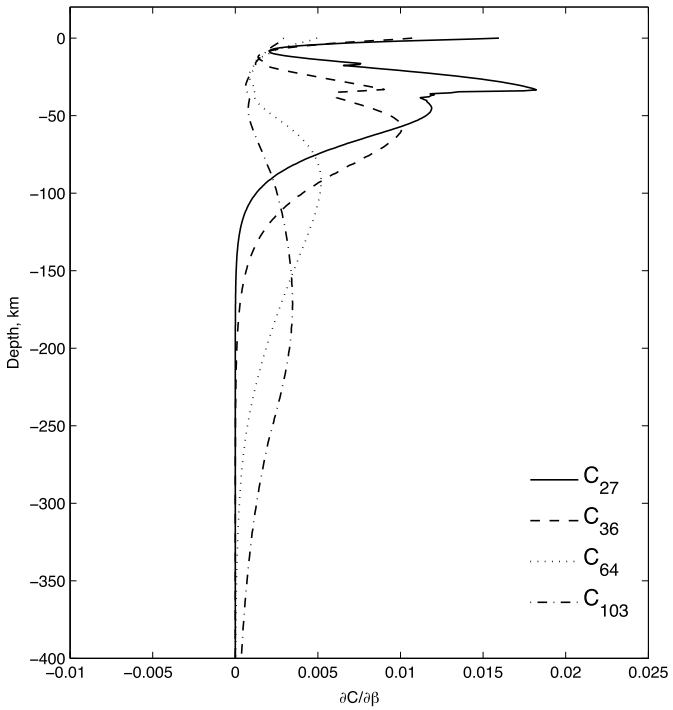

Fig. 4. Partial derivative curves of phase velocity (C) with respect to shear velocity (β) for periods of 27, 36, 64, and 103 s. The wider peak for the 103 s curve is attributed to a shortage of long period data available.

initial 1-D model. Results at shorter periods ($\leq$36 s) show slow velocities along the Terror Rift and along the northern Victoria Land coast. At longer periods ($\geq$64 s), slow velocities are also seen beneath the Erebus Volcanic Province (EVP; Fig. 1) and again beneath northern Victoria Land. The center of the study area shows relatively fast velocities across all periods.

Using the covariance matrix, uncertainty maps for the 2-D inversion were created to estimate the extent of well-resolved portions of our model. Fig. 7 shows the model uncertainty contour map associated with the phase velocity inversion at 36 s period. The uncertainty is minimal in the center of the study area, which is expected due to dense station coverage, and therefore dense raypath coverage. Variance increases towards the periphery of the study area, given a decrease in the station density as well as the damping parameter applied to the outer grid nodes. Again, this damping parameter allowed the outer nodes to absorb peripheral wavefield abnormalities. All resulting phase and shear wave velocity maps are masked at the 0.06 km s^{-1} contour line of the 36 s period uncertainty map. This contour was chosen because it spans the largest area of all periods and best surrounds the densest area of crossing raypaths for all periods.

Resolution at each period was assessed using the model resolution matrix (Fig. 8). The resolution matrices are represented as 2-degree checkers, with each checker alternating between $\pm$5 km s^{-1}. As shown in Fig. 8, each checkerboard is clipped along the 0.06 km s^{-1} uncertainty contour line of the 36 s period uncertainty map, similar to our phase velocity maps. The checkers are well resolved at low to intermediate periods but diminish exponentially past 103 s. The loss of resolution at longer periods limits the depth that can be resolved by the shear wave inversion, consistent with our assessment of the Rayleigh wave phase partial derivatives, discussed previously. It is worth noting that 3-degree checkers were tested in order to assess if larger structure can be resolved at deeper depths, but again, the resolution diminished past 103 s.

3.2. Shear wave velocity

Shear wave velocity maps are shown in Fig. 9, with corresponding cross-sections shown in Fig. 10. As described above, interpretation of the shear wave velocity structure is confined to between ~60 and ~160 km depth. A low velocity zone (LVZ; ~4.24 km s^{-1}) is observed at ~140–160 km depth off the coast and adjacent to Mt. Melbourne. This LVZ extends beneath the continent at shallower depths (Figs. 9–10). Above ~100 km, the LVZ (~4.16–4.24 km s^{-1}) is concentrated beneath the continent, extending beneath northern Victoria Land from near Mt. Melbourne to the northern end of the Hallett Volcanic Province (HVP; Fig. 1). To the south, another prominent LVZ (~4.16–4.24 km s^{-1}) can be seen beneath Ross Island and the EVP, centered at ~150 km depth. The Terror Rift extends between the HVP and the EVP, and also displays seismically slow velocities (~4.24–4.4 km s^{-1}) between ~80–140 km depth. Directly behind the TAMs front, relatively fast seismic velocities (>4.6 km s^{-1}) are observed, which are consistent with stable craton underlying East Antarctica. The boundary between seismically slow and fast velocities, associated with the WARS and the East Antarctic craton, respectively, lies along the coastline parallel to the Terror Rift, slightly extending beneath the continent. In northern Victoria Land, this boundary is directly beneath the TAMs.

4. Discussion

4.1. Low velocity zone sources

The slow upper mantle velocities beneath Ross Island and the Terror Rift observed in our model have also been recognized by previous studies (*e.g.*, Ritzwoller et al., 2001; Morelli and Danesi, 2004; Sieminski et al., 2003; Watson et al., 2006; Lawrence et al., 2006; Hansen et al., 2014), but the source of these low velocities has not been definitively characterized. Several global- and continental-scale tomographic studies have suggested that these slow velocities reflect localized thermal anomalies associated with slow velocities seen across the WARS as a whole (Morelli and Danesi, 2004; Ritzwoller et al., 2001), and some seismic as well as petrologic investigations have attributed such thermal anomalies to plume activity (Kyle et al., 1992; Sieminski et al., 2003; Esser et al., 2004). However, a more recent continental-scale tomographic model (Hansen et al., 2014) indicates that the LVZ beneath Ross Island is a separate feature from other slow anomalies seen beneath West Antarctica and that the Ross Island anomaly is constrained to the upper 200–300 km of the mantle. This is consistent with regional seismic studies in the TAMs, near the McMurdo Dry Valleys, that show little to no evidence for plume structure beneath Ross Island and the Terror Rift (Watson et al., 2006; Lawrence et al., 2006; Reusch et al., 2008).

Alternatively, it has been suggested that volcanism in the EVP and the slow seismic velocities beneath Ross Island result from localized, rift-related decompression melting associated with the Terror Rift (Wannamaker and Stodt, 1996; Rocchi et al., 2005; Karner et al., 2005; Bialas et al., 2007; Huerta and Harry, 2007). Mantle flow may have been directed toward the East Antarctic craton, thereby warming the cratonic lithosphere, and Cenozoic reactivation of Paleozoic tectonic discontinuities may have resulted in localized decompression melting (Rocchi et al., 2003, 2005; Storti et al., 2007; Nardini et al., 2009). Similar to Watson et al. (2006) and Lawrence et al. (2006), our model indicates that the Ross Island and Terror Rift anomalies are focused zones of slow seismic velocity, not broad low velocity features (Fig. 9). Therefore, we interpret these anomalies as areas of focused Cenozoic extension and rift-related decompression melting.

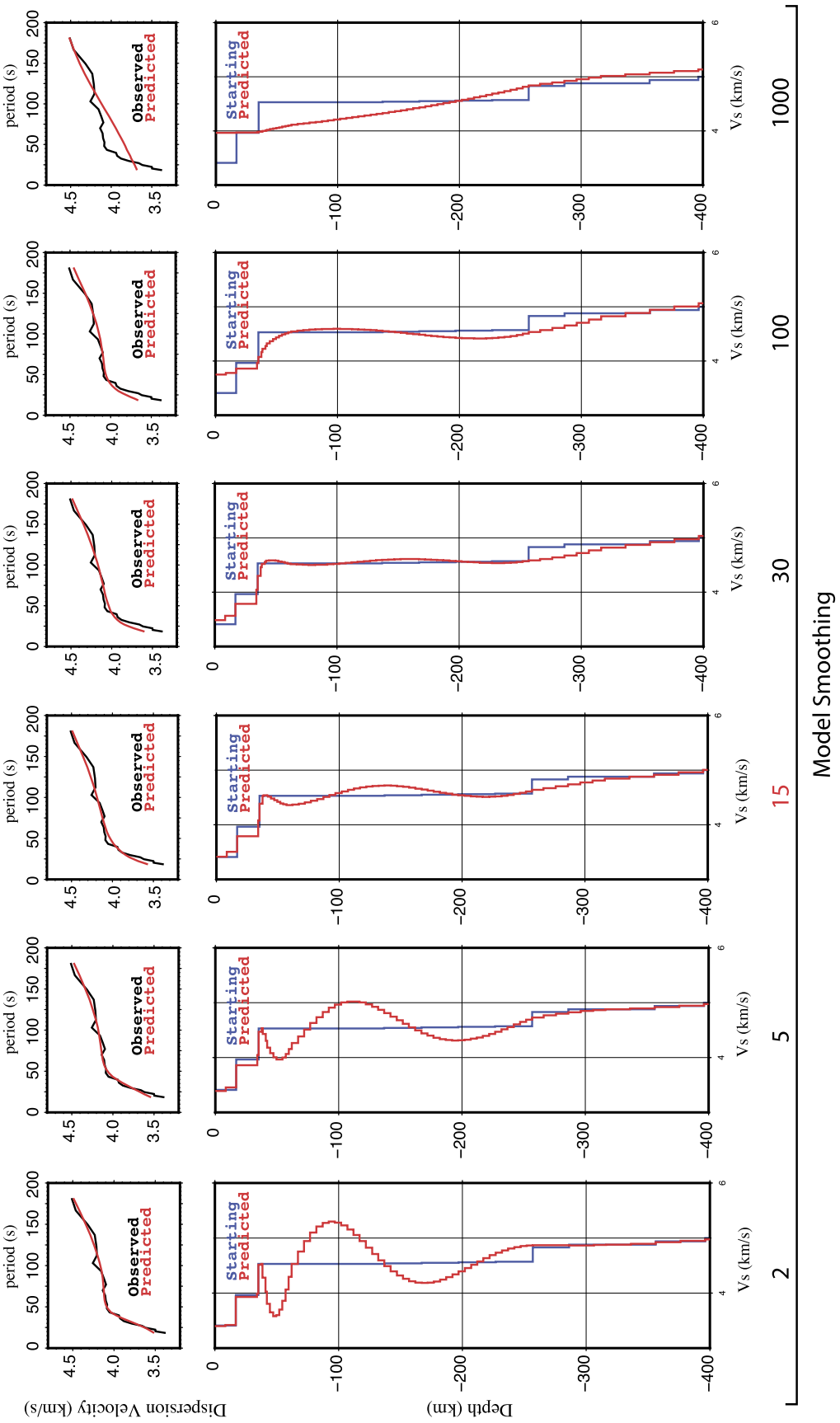

Fig. 5. Model smoothness and data fitting plots for smoothing parameters of 2, 5, 15, 30, 100, and 1000. (Top) The observed Rayleigh wave dispersion curve is in black, and the predicted Rayleigh wave dispersion curve is in red. (Bottom) The resulting velocity models for the inversion using the various smoothing parameters. The blue line is the starting model, and the red line is the predicted model. The numbers below each plot are the smoothing parameters used for that test. A smoothing parameter of 15 (highlighted in red) was chosen for this study. (For interpretation of the references to color in this figure, the reader is referred to the web version of this article.)

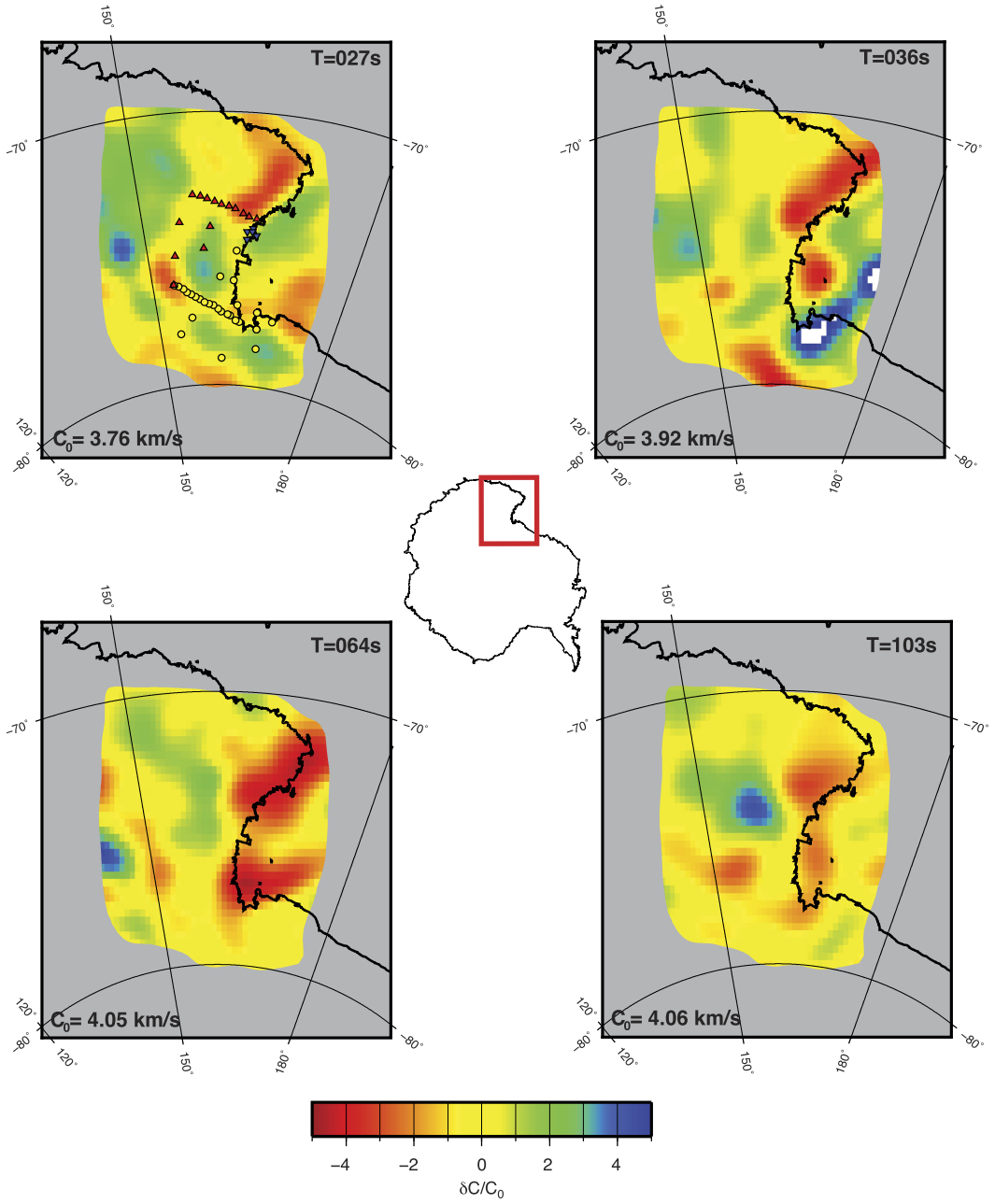

Fig. 6. Phase velocity maps for periods of 27, 36, 64, and 103 s. Plotted values are percent deviations from the initial 1-D model at the same period ($\delta C/C_0$). The initial 1-D phase velocity value is shown on the lower left in each panel. Station symbols, shown on the 27 s period panel, are the same as in Fig. 1.

The LVZ beneath northern Victoria Land highlighted in our model (Figs. 9–10) is a new feature that has not been observed at a regional scale. As discussed previously, this LVZ appears to extend to a depth of ∼160 km depth off the coast and adjacent to Mt. Melbourne, and it then extends inland and vertically upwards, concentrating at depths above ∼100 km. It should be noted that this feature may extend deeper, but our model is not well resolved past ∼160 km. However, the continental-scale model of Hansen et al. (2014), which also included TAMNNET data, does not show slow velocities extending past about ∼200–300 km depth; therefore, it is likely that the slow velocities seen in our model are constrained to the upper mantle. This observation is not consistent with investigations that suggest a deep-seated mantle upwelling beneath the northern TAMs (*e.g.*, Sieminski et al., 2003; Faccenna et al., 2008; Austermann et al., 2015).

The LVZ extends vertically in a west–northwest direction from offshore to beneath the coastline (Fig. 10), which may result from a lateral force associated with the absolute direction of plate motion (Fig. 9). However, comparable structure is not observed in the Ross Island or Terror Rift anomalies further to the south. Alternatively, we suggest that the change in the LVZ orientation indicates that the slow mantle material is ascending along and following a path of least resistance. For instance, Hansen et al. (2016) recently showed that the crust may be locally thicker beneath the northern TAMs, in close proximity to where the LVZ orientation changes. This may direct the slow mantle material beneath northern Victoria Land, as seen in our model.

The signature of the Victoria Land LVZ at ∼140–160 km depth is similar to that seen beneath Ross Island, and it is noteworthy that the two LVZs appear to be connected by relatively slow velocities along the Terror Rift (Fig. 10). Similar structure to that seen

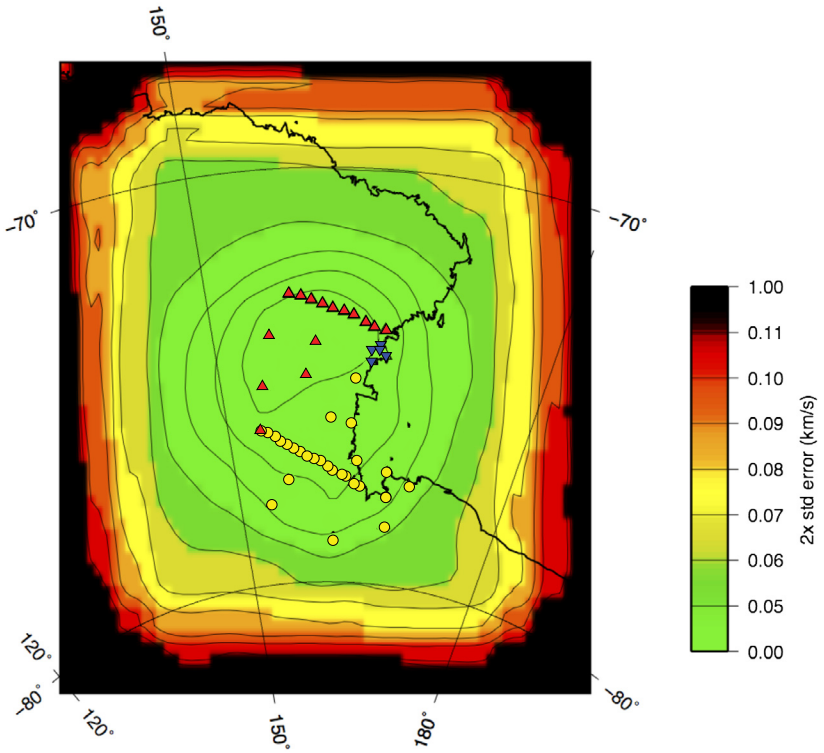

Fig. 7. Model uncertainty for phase velocities at a period of 36 s. The green area lies within the 0.06 km s^{-1} uncertainty line. This contour is used in Figs. 6, 8, and 9 to crop the region displayed. Station symbols are the same as in Fig. 1. (For interpretation of the references to color in this figure, the reader is referred to the web version of this article.)

in our model is also observed, for instance, in surface wave tomographic images from the Gulf of California, where it has been suggested that connected pockets of low velocity material in the upper mantle are best attributed to buoyancy-driven upwelling and melting, triggered by an extensional episode (Wang et al., 2009). Our pattern of low velocities is consistent with this interpretation, implying a continuance of rift-related decompression melting along the TAMs front at the northern end of the Terror Rift. Further, geochemical and petrological studies of other rifted environments indicate that partial melting can occur at ∼150 km depth if the proper mantle conditions exist (*i.e.*, volatiles are present) and that upwelling from this point of initial melt primarily follows paths of mantle weakness to shallower depths, where reinvigorated, intensified melting transpires, often at ∼50–60 km depth (Asimow et al., 2001). This could also explain both the trend and amplitude of the low velocity anomalies observed in our model, including the slow velocities observed above ∼100 km beneath northern Victoria Land.

4.2. TAMs uplift in northern Victoria Land

As outlined in the introduction, proposed uplift models for the TAMs include: (1) upward flexure along the edge of the East Antarctic craton due to thermal conduction from the adjacent WARS (Stern and ten Brink, 1989; ten Brink et al., 1997), (2) basin subsidence and rift flank uplift requiring a thick crustal root (Studinger et al., 2004; Karner et al., 2005), and (3) a hybrid model in which uplift results from a combination of thermal buoyancy, local crustal isostasy, and erosional unloading (Lawrence et al., 2006). Crustal studies based on S-wave receiver functions indicate that while the northern TAMs may be underlain by slightly thicker crust, a crustal root is not a consistent, along-strike feature beneath the mountain range (Hansen et al., 2012, 2016). Small-scale, local crustal thickness variations may provide some isostatic buoyancy for the TAMs, but this does not appear to be a major contributing factor to the TAMs uplift.

Similar to Watson et al. (2006) and Lawrence et al. (2006), our model shows that the boundary between fast and slow seismic velocities lies ∼60–90 km inland of the coast, parallel to the Terror Rift, beneath the TAMs (Fig. 9). This is consist with a thermal load, as suggested by Stern and ten Brink (1989) and ten Brink et al. (1997), which would thermally modify the TAMs lithosphere and cause flexural uplift. However, our model illustrates that the upper mantle structure beneath the northern TAMs is somewhat different. Here, low velocity material is concentrated at shallow (<∼100 km) depths beneath the mountain range. Such an anomaly would have an even more pronounced thermal buoyancy affect on this portion of the TAMs, and indeed, the bedrock topography within the northern TAMs is significantly higher than that along the portion of the TAMs parallel to the Terror Rift (Fig. 10). The high topography in the northern TAMs is situated directly above the shallow LVZ. Watson et al. (2006) suggested that heating of the TAMs lithosphere may be variable along-strike the mountain front, and our results provide good evidence that this seems to be the case. As discussed in section 4.1, this variable heating is likely due to linked pockets of buoyancy-driven upwelling associated with extension along the Terror Rift, with intensified melting at shallower depths.

4.3. Northern TAMs uplift and volcanism

Our results may also help to explain the source of young, Cenozoic volcanic rocks seen within both the EVP and the HVP (Fig. 1). The exposed volcanic rocks in both of these areas directly overlie the LVZs highlighted in our model (Fig. 9), providing strong evidence that the LVZs serve as the sources for the surface magmatism. Our tomographic findings best match a rift-related isotopic signature (Rocholl et al., 1995), as opposed to a HIMU mantle source (Rocchi et al., 1995, 2005). Previous

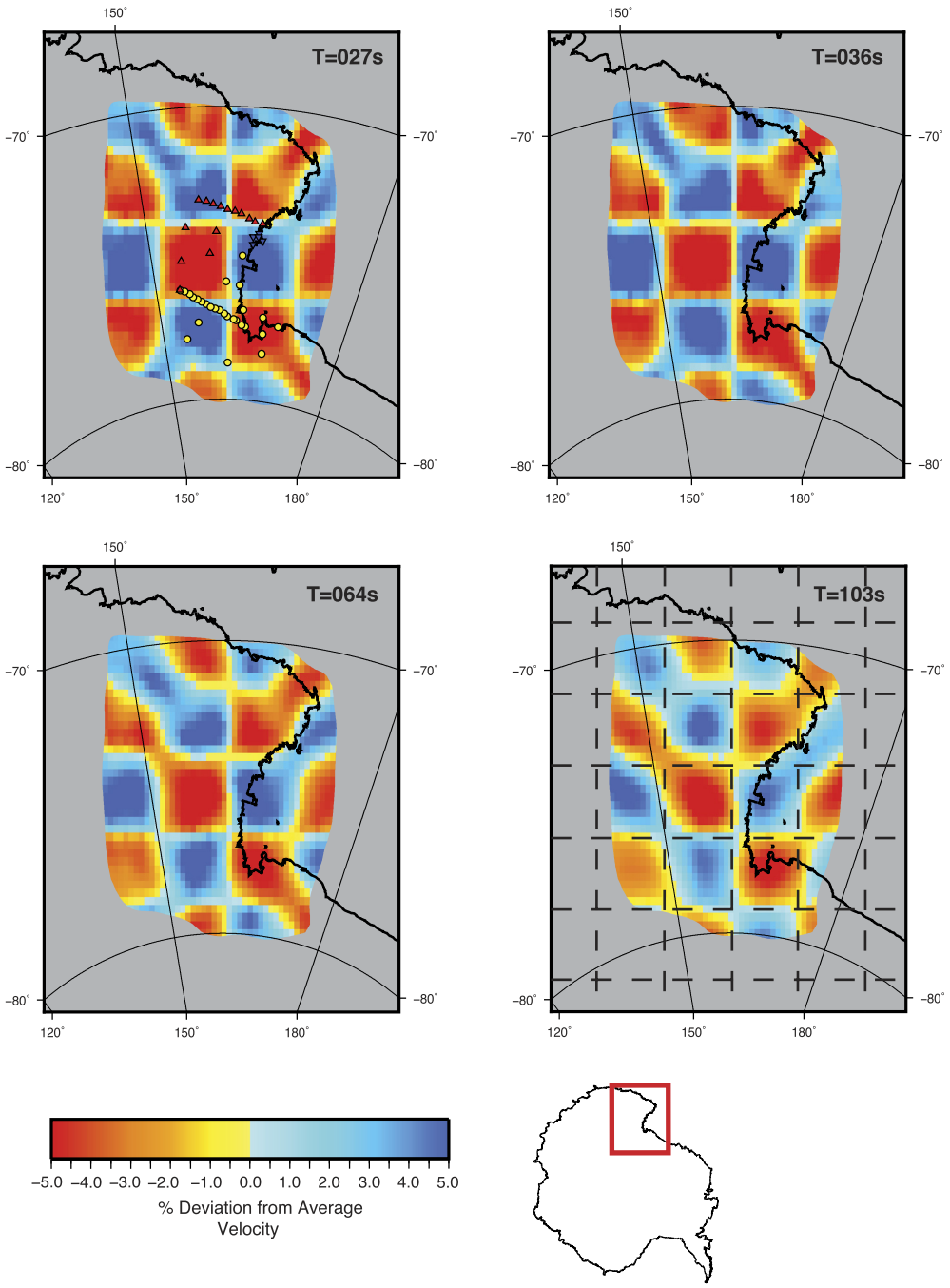

Fig. 8. Resolution tests at periods of 27, 36, 64, and 103 s. All input checkers are 2-degree squares, and their locations are shown by the dashed lines in the 103 s period map. Station symbols, shown on the 27 s period panel, are the same as in Fig. 1.

studies have dated the volcanic rocks, yielding ages of 0–15 Ma (Rocchi et al., 2002 and references therein); therefore, it is plausible that volcanic activity continues to the present. The distribution of the Cenozoic volcanic rocks provides another line of evidence that the LVZs are associated with warm regions of partial melt within the upper mantle, which would provide a thermal load to support the TAMs uplift (Stern and ten Brink, 1989; ten Brink et al., 1997).

5. Conclusions

Using recently acquired seismic data and the two-plane wave tomography method, we have developed a new model of the upper mantle velocity structure beneath the northern TAMs. Our results show low velocities beneath Ross Island and the Terror Rift, similar to previous regional models (Watson et al., 2006; Lawrence et al., 2006), but we also highlight a previously unrecognized LVZ beneath the northern TAMs and Victoria Land. This LVZ extends to ∼160 km depth and extends vertically upward to ∼60 km depth. Slow seismic velocities along the Terror Rift connect the LVZs seen beneath both Ross Island and beneath northern Victoria Land. We suggest that the LVZs reflect rift-related decompression melting and Cenozoic extension. The thermal load provided by these anomalies helps to support the uplift of the TAMs and is consistent with a flexural origin (Stern and ten Brink, 1989; ten Brink et al., 1997). However, we also propose that heating along the TAMs front is variable and that the shallow LVZ beneath northern Victoria Land results in a greater thermal buoyancy effect

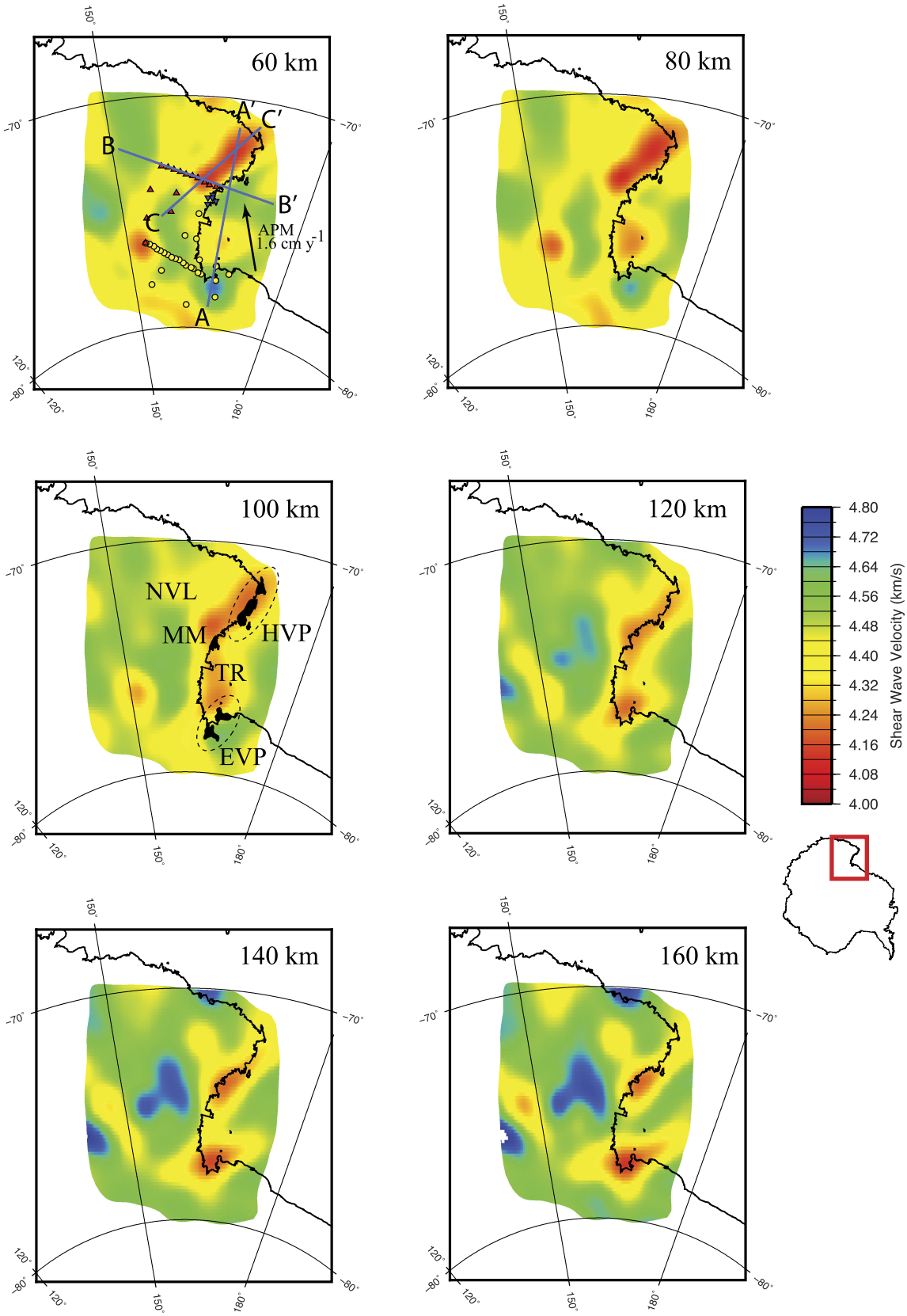

Fig. 9. Shear wave velocities at 60, 80, 100, 120, 140, and 160 km depths. Station symbols (same as Fig. 1) and cross-section locations (Fig. 10) are shown on the 60 km depth panel. Average plate motion (APM) is also shown on that panel by the black arrow. Key volcanic areas are shown on the 100 km depth panel. MM: Mt. Melbourne, HVP: Hallett Volcanic Province, EVP: Erebus Volcanic Province, TR: Terror Rift, NVL: Northern Victoria Land.

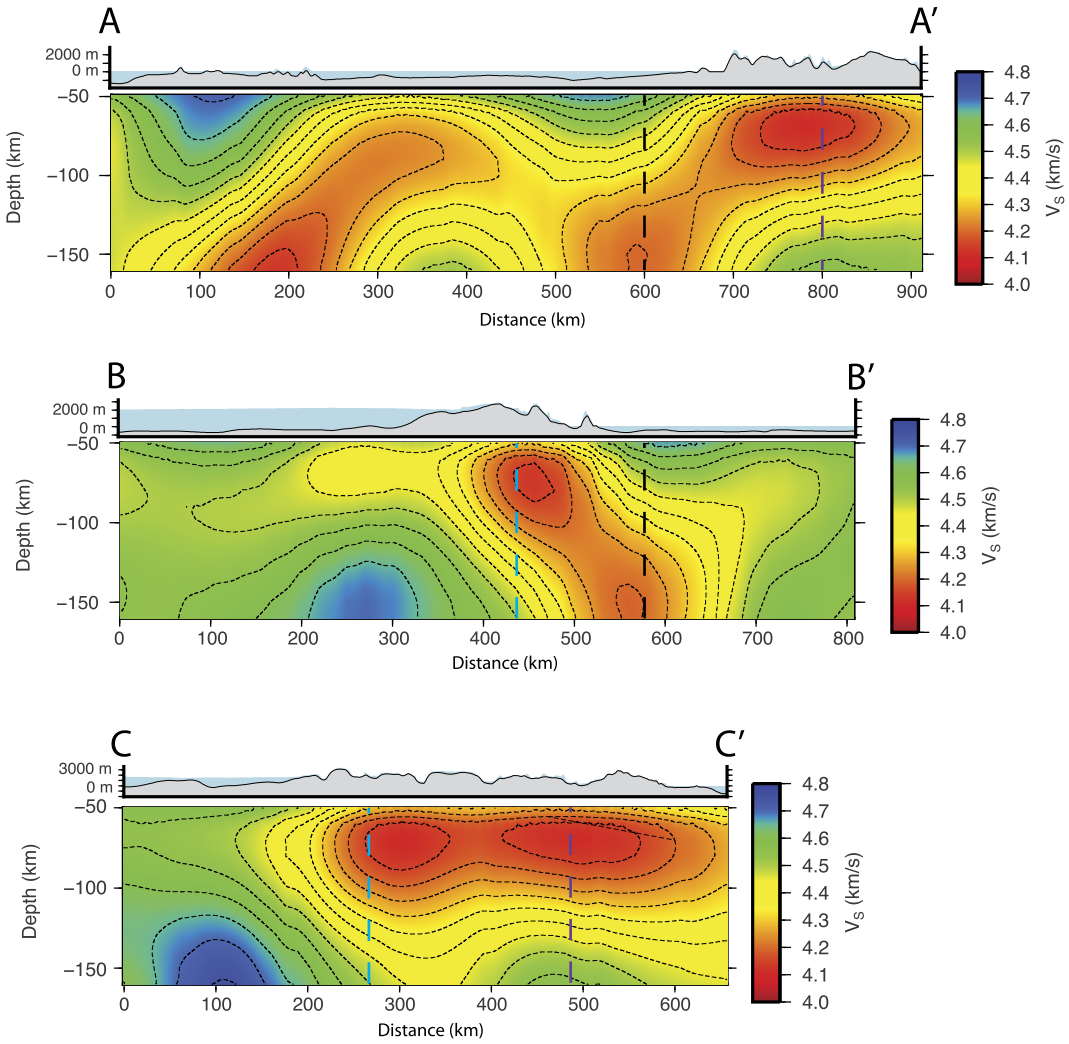

Fig. 10. Cross-sections along profiles A–A′, B–B′, and C–C′ (locations shown on Fig. 9), with bedrock (gray) and ice (blue) topography from BEDMAP2 (Fretwell et al., 2013) shown above. Dashed lines show where the cross-sections intersect one another, matching along the black, blue, and purple dashed lines. (For interpretation of the references to color in this figure, the reader is referred to the web version of this article.)

and hence higher surface topography in the northern TAMs. Our model may also explain the source of 0–15 Ma exposed volcanic rocks in the EVP and HVP.

Acknowledgements

We thank the TAMNNET, TAMSEIS, and KPSN field teams responsible for maintaining the instrumentation and for collecting the data that has been used in our study, as well as the staff at IRIS-PASSCAL, Ken Borek Air, and McMurdo Station for their technical and logistical support. We also thank Dr. Anya Reading and an anonymous reviewer for their thorough critiques of this manuscript. Data management handling was provided by the IRIS-DMC. The facilities of the IRIS Consortium are supported by the National Science Foundation (NSF) under cooperative agreement EAR-1063471, the NSF Office of Polar Programs, and the Department of Energy National Nuclear Security Administration. Funding for this research was provided by the NSF (grant number ANT-1148982) and by Korean grant PM15020.

References

Adams, A., Nyblade, A., Weeraratne, D., 2012. Upper mantle shear wave velocity structure beneath the East African plateau: evidence for a deep, plateauwide low velocity anomaly. Geophys. J. Int. 189, 123–142.

Asimow, P.D., Hirschmann, M.M., Stolper, E.M., 2001. Calculation of peridotite partial melting from thermodynamic models of mineral and melts, IV. Adiabatic decompression and the composition and mean properties of mid-ocean ridge basalts. J. Petrol. 42, 963–998.

Austermann, A., Pollard, D., Mitrovica, J.X., Moucha, R., Forte, A.M., DeConto, R.M., Rowley, D.B., Raymo, M., 2015. The impact of dynamic topography change on Antarctic ice sheet stability during the mid-Pliocene warm period. Geology 43, 927–930.

Bannister, S., Leitner, J.Y., Kennett, B.L.N., 2003. Variations in crustal structure across the transition from West to East Antarctica, Southern Victoria Land. Geophys. J. Int. 155, 870–884.

Barrett, P.J., 1991. The Devonian to Jurassic Beacon Supergroup of the Tansantarctic Mountains and correlatives in other parts of Antarctica. In: The Geology of Antarctica. In: Oxford Monographs on Geology and Geophysics, vol. 17, pp. 120–152.

Bialas, R.W., Buck, W.R., Studinger, M., Fitzgerald, P.G., 2007. Plateau collapse model for the Transantarctic Mountains–West Antartctic Rift System: insights from numerical experiments. Geology 35, 687–690.

Borg, S.G., DePaolo, D.J., Smith, B.M., 1990. Isotopic structure and tectonics of the central Transantarcic Mountains. J. Geophys. Res. 95, 6647–6667.

Di Vincenzo, G., Bracciali, L., Del Carlo, P., Panter, K., Rocchi, S., 2010. ^{40}Ar–^{39}Ar dating of volcanogenic products from the AND-2A core (ANDRILL Southern McMurdo Sound Project, Antarctica): correlations with the Erebus Volcanic Province and implications for the age model of the core. Bull. Volcanol. 72, 487–505.

Dziewonski, A.M., Anderson, D.L., 1981. Preliminary reference Earth model. Phys. Earth Planet. Inter. 25, 297–356.

Esser, R.P., Kyle, P.R., McIntosh, W.C., 2004. $^{40}Ar/^{39}Ar$ dating of the eruptive history of Mount Erebus, Antarctica: volcano evolution. Bull. Volcanol. 66, 671–686.

Faccenna, C., Rossetti, F., Becker, T.W., Danesi, S., Morelli, A., 2008. Recent extension driven by mantle upwelling beneath the Admiralty Mountains (East Antarctica). Tectonics 27. http://dx.doi.org/10.1029/2007TC002197.

Fitzgerald, P., 2002. Tectonics and landscape evolution of the Antarctic plate since the breakup of Gondwana, with an emphasis on the West Antarctic Rift System and the Transantarctic Mountains. Bull. R. Soc. N. Z. 35, 453–469.

Forsyth, D.W., Li, A., 2005. Array analysis of two-dimensional variations in surface wave phase velocity and azimuthal anisotropy in the presence of multipathing interference. In: Seismic Earth: Array Analysis of Broadband Seismograms. In: Geophysical Monograph Series, vol. 157, pp. 81–97.

Fretwell, P., et al., 2013. BEDMAP2: improved ice bed, surface and thickness datasets for Antarctica. Cryosphere 7, 375–393.

Hansen, S.E., Julia, J., Nyblade, A.A., Pyle, M.L., Wiens, D.A., Anandakrishnan, S., 2009. Using S wave receiver functions to estimate crustal structure beneath ice sheets: an application to the Transantarctic Mountains and East Antarctic craton. Geochem. Geophys. Geosyst. 10, Q08014.

Hansen, S.E., Nyblade, A.A., Benoit, M.H., 2012. Mantle structure beneath Africa and Arabia from adaptively parameterized P-wave tomography: implications for the origin of Cenozoic Afro-Arabian tectonism. Earth Planet. Sci. Lett. 319–320, 23–34.

Hansen, S.E., Graw, J.H., Kenyon, L.M., Nyblade, A.A., Wiens, D.A., Aster, R.C., Huerta, A.D., Anandakrishnan, S., Wilson, T., 2014. Imaging the Antarctic mantle using adaptively parameterized P-wave tomography: evidence for heterogeneous structure beneath West Antarctica. Earth Planet. Sci. Lett. 408, 66–78.

Hansen, S.E., Reusch, A.M., Parker, T., Bloomquist, D.K., Carpenter, P., Graw, J.H., Brenn, G.R., 2015. The Transantarctic Mountains Northern Network (TAMNNET): deployment and performace of a seismic array in Antarctica. Seismol. Res. Lett. 86. http://dx.doi.org/10.1785/0220150117.

Hansen, S.E., Kenyon, L.M., Graw, J.H., Park, Y., Nyblade, A., 2016. Crustal structure beneath the Northern Transantarctic Mountains and Wilkes Subglacial Basin: implications for tectonic origins. J. Geophys. Res. 121. http://dx.doi.org/10.1002/2015JB012325.

Huerta, A.D., Harry, D.L., 2007. The transition from diffuse to focused extension: modeled evolution of the West Antarctic Rift system. Earth Planet. Sci. Lett. 255, 133–147.

Julià, J., Ammon, C.J., Herrmann, R.B., Correig, A.M., 2000. Joint inversion of receiver function and surface wave dispersion observations. Geophys. J. Int. 143, 99–112.

Karner, G.D., Studinger, M., Bell, R.E., 2005. Gravity anomalies of sedimentary basins and their mechanical implications: application to the Ross Sea basins, West Antarctica. Earth Planet. Sci. Lett. 235, 577–596.

Kennett, B.L.N., Engdahl, E.R., Buland, R., 1995. Constraints on seismic velocities in the Earth from traveltimes. Geophys. J. Int. 122, 108–124.

Kyle, P.R., 1990. McMurdo volcanic group, Western Ross Embayment. In: LeMasurier, W.E., Thomson, J.W. (Eds.), Volcanoes of the Antarctic Plate and Southern Oceans. In: Antarct. Res. Ser., vol. 48. AGU, Washington, DC, pp. 19–25.

Kyle, P.R., Moore, J.A., Thrilwall, M.F., 1992. Petrologic evolution of anothroclase phonolite lavas at Mt. Erebus, Ross Island, Antarctica. J. Petrol. 33, 849–875.

Lawrence, J.F., Wiens, D.A., Nyblade, A.A., Anandakrishnan, S., Shore, P.J., Voigt, D., 2006. Crust and upper mantle structure of the Transantarctic Mountains and surrounding regions from receiver functions, surface waves, and gravity: implications for uplift models. Geochem. Geophys. Geosyst. 7, 23.

Li, A., Forsyth, D.W., Fischer, K.M., 2003. Shear velocity structure and azimuthal anisotropy beneath eastern North America from Rayleigh wave inversion. J. Geophys. Res. 108 (B8), 2362.

Morelli, A., Danesi, S., 2004. Seismological imaging of the Antarctic continental lithosphere: a review. Glob. Planet. Change 42, 155–165.

Nardini, I., Armienti, P., Rocchi, S., Dallai, L., Harrison, D., 2009. Sr–Nd–Pb–He–O isotope and geochemical contstraints on the genesis of Cenozoic magmas from the West Antarctic Rift. J. Petrol. 50, 1359–1375.

Orlando, A., Conticelli, S., Armienti, P., Borrini, D., 2000. Experimental study on a basanite from the McMurdo Volcanic group, Antarctica: inference on its mantle source. Antarct. Sci. 12, 105–116.

Park, Y., Yoo, H.J., Lee, W.S., Lee, J., Kim, Y., Lee, S., Shin, D., Park, H., 2014. Deployment and performance of a broadband seismic network near the new Korean Jang Bogo Research Station, Terra Nova Bay, East Antarctica. Seismol. Res. Lett. 85. http://dx.doi.org/10.1785/0220140107.

Reusch, A.M., Nyblade, A.A., Benoit, M.H., Wiens, D.A., Anandakrishnan, S., Voigt, D., Shore, P.J., 2008. Mantle transition zone thickness beneath Ross Island, the Transantarctic Mountains and East Antarctica. Geophys. Res. Lett. 35. http://dx.doi.org/10.1029/2008GL033873.

Ritzwoller, M.H., Shapiro, N.M., Levshin, A.L., Leahy, G.M., 2001. Crustal and upper mantle structures beneath Antarctica and surrounding oceans. J. Geophys. Res. 106, 30645–30670.

Rocchi, S., Armienti, P., D'Orazio, M., Tonarini, S., Wijbrans, J., Di Vincenzo, G., 2002. Cenozoic magmatism in the western Ross Embayment: role of mantle plume vs. plate dynamics in the development of the West Antarctic Rift System. J. Geophys. Res. 107.

Rocchi, S., Storti, F., Di Vincenzo, G., Rosetti, F., 2003. Intraplate strike-slip tectonics as an alternative to mantle plume activity for the Cenozoic rift magmatism in the Ross Sea region, Antarctica. In: Storti, F., Holdsworth, R.E., Salvini, F. (Eds.), Intraplate Strike-Slip Deformation Belts. Geol. Soc. (Lond.) Spec. Publ. 210, 145–158.

Rocchi, S., Armienti, P., Di Vincenzo, G., 2005. No plume, no rift magmatism in the West Antarctica Rift. In: Foulger, G.R., Natland, J.H., Presnall, D.C., Anderson, D.L. (Eds.), Plates, Plumes, and Paradigms. In: Spec. Pap., Geol. Soc. Am., vol. 388, pp. 435–447.

Rocholl, A.M., Stein, M., Molzahn, M., Hart, S.R., Wörner, G., 1995. Geochemical evolution of rift magmas by progressive tapping of stratified mantle source beneath the Ross Sea Rift, Northern Victoria Land, Antarctica. Earth Planet. Sci. Lett. 131, 207–224.

Sieminski, A., Debayle, E., Leveque, J., 2003. Seismic evidence for deep low-velocity anomalies in the transition zone beneath West Antarctica. Earth Planet. Sci. Lett. 216, 645–661.

Stern, T.A., ten Brink, U.S., 1989. Flexural uplift of the Transantarctic Mountains. J. Geophys. Res. 94, 10315–10330.

Storti, F., Salvini, F., Rossetti, F., Phipps Morgan, J., 2007. Intraplate termination of transform faulting within the Antarctic continent. Earth Planet. Sci. Lett. 260, 115–126.

Storti, S., Balestrieri, M.L., Balsamo, F., Rossetti, F., 2008. Structural and thermochronological constraints to the evolution of the West Antarctic Rift System in central Victoria Land. Tectonics 27. http://dx.doi.org/10.1029/2006TC002066.

Studinger, M., Bell, R.E., Buck, W.R., Karner, G.D., Blankenship, D.D., 2004. Sub-ice geology inland of the Transantarctic Mountains in light of new aerogeophysical data. Earth Planet. Sci. Lett. 220, 391–408.

ten Brink, U.S., Hackney, R.I., Bannister, S., Stern, T.A., Makovsky, Y., 1997. Uplift of the Transantarctic Mountains and the bedrock beeath the East Antarctic ice sheet. J. Geophys. Res. 102, 27603–27621.

Wang, Y., Forsyth, D.W., Savage, B., 2009. Convective upwelling in the mantle beneath the Gulf of California. Nature 462, 499–501.

Wannamaker, P.E., Stodt, J.A., 1996. Dormant state of rifting below the Byrd Subglacial Basin, West Antarctica, implied by magnetotelluric (MT) profiling. Geophys. Res. Lett. 23, 2983–2986.

Watson, T., Nyblade, A., Wiens, D.A., Anandakrishnan, S., Benoit, M., Shore, P.J., Voigt, D., VanDecar, J., 2006. P and s velocity structure of the upper mantle beneath the Transantarctic Mountains, East Antarctic craton, and Ross Sea from travel time tomography. Geochem. Geophys. Geosyst. 7, 17.

Yang, Y., Forsyth, D.W., 2006a. Regional tomographic inversion of the amplitude and phase of Rayleigh waves with 2-D sensitivity kernels. Geophys. J. Int. 166, 1148–1160.

Yang, Y., Forsyth, D.W., 2006b. Rayleigh wave phase velocities, small-scale convection, and azimuthal anisotropy beneath southern California. J. Geophys. Res. 111, B07306.

Yu, G., Mitchell, B.J., 1979. Regionalized shear velocity models of the Pacific upper mantle from observed Love and Rayleigh wave dispersion. Geophys. J. Int. 57, 311–341.

Zhou, Y., Dahlen, F.A., Nolet, G., 2004. Three-dimensional sensitivity kernels for surface wave observables. Geophys. J. Int. 158, 142–168.